PHYSICS

Enabling propagation of anisotropic polaritons along forbidden directions via a topological transition

J. Duan[1,2]*, G. Álvarez-Pérez[1,2]*, K. V. Voronin[3], I. Prieto[4], J. Taboada-Gutiérrez[1,2], V. S. Volkov[3], J. Martín-Sánchez[1,2†], A. Y. Nikitin[5,6†], P. Alonso-González[1,2†]

Polaritons with directional in-plane propagation and ultralow losses in van der Waals (vdW) crystals promise unprecedented manipulation of light at the nanoscale. However, these polaritons present a crucial limitation: their directional propagation is intrinsically determined by the crystal structure of the host material, imposing forbidden directions of propagation. Here, we demonstrate that directional polaritons (in-plane hyperbolic phonon polaritons) in a vdW crystal (α-phase molybdenum trioxide) can be directed along forbidden directions by inducing an optical topological transition, which emerges when the slab is placed on a substrate with a given negative permittivity (4H–silicon carbide). By visualizing the transition in real space, we observe exotic polaritonic states between mutually orthogonal hyperbolic regimes, which unveil the topological origin of the transition: a gap opening in the dispersion. This work provides insights into optical topological transitions in vdW crystals, which introduce a route to direct light at the nanoscale.

INTRODUCTION

Phonon polaritons (PhPs), hybrid electromagnetic waves arising from the strong coupling of photons and optical phonons in polar dielectrics, in materials consisting of atomic planes bonded by weak van der Waals (vdW) forces (vdW materials) hold great promises for infrared nanophotonics (*1–3*), as they feature deep subwavelength confinement and ultralow loss propagation. In particular, PhPs in so-called hyperbolic media (HPhPs) exhibit an extremely anisotropic dispersion, that is, their isofrequency curve (IFC), a slice of the dispersion in momentum-frequency space by a plane of a constant frequency ω_0, describes a hyperbola-like curve (*4–8*). Consequently, the propagation of HPhPs is strongly anisotropic, manifesting itself in a very peculiar fashion. For instance, HPhPs launched by a point source feature concave wavefronts and strong directionality due to the enormous density of optical states at specific wave vectors (along the IFC asymptotes). This exotic polaritonic propagation was first reported for out-of-plane HPhPs in the uniaxial crystal hexagonal boron nitride (*9–11*), showing remarkable potential for applications in photonics (*12*), specifically for subdiffractional focusing (*13*, *14*) and sensing via strong coupling with organic molecules (*15*). More recently, in-plane HPhPs have been found in the biaxial vdW crystals α-phase molybdenum trioxide (α-MoO$_3$) (*16*, *17*) and α-phase vanadium pentaoxide (α-V$_2$O$_5$) (*18*), opening the door to study directly on the crystal surfaces extraordinary optical phenomena stemming from the low-loss directional propagation of HPhPs. Nevertheless, the direction of propagation of HPhPs in naturally hyperbolic media is difficult to manipulate, since it is predefined by

the intrinsic anisotropy of the crystal, which forbids propagation along certain directions. This inherent limitation reduces the potential and versatility of HPhPs for applications requiring specific propagation directions of the electromagnetic energy flow at the nanoscale, such as coupling between quantum emitters (*19*, *20*) or heat management (*21*). Specifically, in-plane hyperbolic polaritons can only propagate along directions contained between the asymptotes of their IFC in the (k_x, k_y) plane, i.e., within the hyperbolic sectors $|\tan(k_x/k_y)| < \sqrt{(-\varepsilon_y/\varepsilon_x)}$, where ε_x and ε_y are the in-plane permittivities of the hyperbolic medium and k_x and k_y are the in-plane components of the wave vector. Therefore, any engineering, manipulation, or reorientation of the IFC will obviously have a marked effect on the directional propagation of hyperbolic polaritons in real space. Recently, attempts to manipulate this anisotropic propagation of polaritons in vdW crystals have been carried out, either by assembling crystal heterostructures (*22*) or by fabricating metasurfaces (*23*) and twisted bilayers (*24–27*). The latter has even demonstrated that the propagation of HPhPs can be guided along one specific direction. However, despite this extraordinary progress, a solution to overcome the existence of intrinsically forbidden directions of propagation of HPhPs has so far remained elusive, even from a theoretical point of view. Here, we theoretically predict and experimentally demonstrate that a reorientation of the IFC of hyperbolic polaritons in a biaxial slab can be engineered to allow propagation along forbidden directions. This is caused by a low-loss topological transition of the IFC, which is naturally induced when the biaxial slab is placed on a substrate with a given negative permittivity. In particular, we demonstrate that the direction of propagation of in-plane HPhPs in an α-MoO$_3$ slab can be rotated by 90° (and thus occur along intrinsically forbidden directions in the studied spectral range) by placing the slab on a 4H-SiC substrate. The low-loss character of the topological transition allows us to experimentally reveal exotic polaritonic intermediate states, in which HPhPs propagate along mutually orthogonal directions. By theoretically analyzing these states, we unveil the exotic topological origin of this transition, characterized by a gap opening in the polaritonic dispersion.

[1]Department of Physics, University of Oviedo, Oviedo 33006, Spain. [2]Center of Research on Nanomaterials and Nanotechnology, CINN (CSIC-Universidad de Oviedo), El Entrego 33940, Spain. [3]Center for Photonics and 2D Materials, Moscow Institute of Physics and Technology, Dolgoprudny 141700, Russia. [4]Institute of Science and Technology Austria, am Campus 1, Klosterneuburg 3400, Austria. [5]Donostia International Physics Center (DIPC), Donostia-San Sebastián 20018, Spain. [6]IKERBASQUE, Basque Foundation for Science, Bilbao 48013, Spain.
*These authors contributed equally to this work.
†Corresponding author. Email: pabloalonso@uniovi.es (P.A.); alexey@dipc.org (A.Y.N.); javiermartin@uniovi.es (J.M.)

RESULTS AND DISCUSSION

To elaborate on the theoretical conditions upon which this reorientation of the directional propagation of HPhPs can take place, let us start analyzing the general case of a biaxial slab embedded between two semi-infinite isotropic media with dielectric permittivities ε_1 and ε_3. Without loss of generality, we assume the representative dielectric functions $Re(\varepsilon_x) < 0$, $Re(\varepsilon_y)$, $Re(\varepsilon_z) > 0$, in analogy with the convention for biaxial vdW materials in which in-plane HPhPs have been reported to date, such as α-MoO$_3$ (16, 17, 28) and α-V$_2$O$_5$ (18). Propagation of in-plane HPhPs occurs within hyperbolic sectors centered along the direction with negative permittivity, i.e., the x axis. The dispersion relation of polaritons in a biaxial slab (considering the layers stacked along the z axis) reads (29)

$$k(\omega) = \frac{\rho}{d}\left[\arctan\left(\frac{\varepsilon_1 \rho}{\varepsilon_z}\right) + \arctan\left(\frac{\varepsilon_3 \rho}{\varepsilon_z}\right) + \pi l\right], l = 0, 1, 2\ldots, \quad (1)$$

where d is the thickness of the biaxial slab, k is the in-plane wave vector ($k^2 = k_x^2 + k_y^2$), α is the angle between the x axis and k, $\rho = i\sqrt{(\varepsilon_z/(\varepsilon_x \cos^2\alpha + \varepsilon_y \sin^2\alpha))}$, and l is the mode index. Setting $k_y = 0$ (or $\alpha = 0$) in Eq. 1, we find that conventional propagation of in-plane hyperbolic polaritons centered along the x axis is allowed when $Re(\varepsilon_1) + Re(\varepsilon_3) > 0$ (see details in section S1). We also find that propagation of hyperbolic polaritons is allowed along the dielectric y axis—i.e., physical solutions of Eq. 1 for $\alpha = \pi/2$—, initially a nonpolaritonic direction (16, 17, 28), when the condition $Re(\varepsilon_1) + Re(\varepsilon_3) < 0$ is fulfilled (see section S1). Therefore, these results predict a 90° reorientation of the hyperbolic IFC of polaritons in a biaxial slab in the neighborhood of $Re(\varepsilon_1) + Re(\varepsilon_3) = 0$. We note that although propagation of polaritons along any given in-plane direction is found for both α and $\alpha + \pi$, for simplicity, we show the dispersion only for α, which corresponds to waves propagating with positive Poynting vector **S**.

This prediction can be addressed using natural materials, such as the biaxial vdW semiconductor α-MoO$_3$ placed on top of the polar crystal 4H-SiC, since α-MoO$_3$ supports low-loss in-plane HPhPs in its reststrahlen band (28) (821 to 963 cm^{-1}) along which 4H-SiC has negative permittivity (30) ($Re(\varepsilon_3) < 0$ from 797 to 970 cm^{-1}) (see section S2). The permittivity of 4H-SiC attains a value $Re(\varepsilon_3) = -1$ at the surface optical (SO) phonon frequency $\omega_{SO} = 943$ cm^{-1} (see section S2), where it thus approximately fulfills the critical condition derived for the rotation of the IFC, $Re(\varepsilon_1) + Re(\varepsilon_3) = 0$, when air is considered as superstrate ($\varepsilon_1 = 1$). To explore this possibility, we compare the analytical dispersion of HPhPs in a slab of α-MoO$_3$ when it is placed on top of a 4H-SiC substrate and on top of a commonly used dielectric substrate, such as SiO$_2$, where the condition $Re(\varepsilon_1) + Re(\varepsilon_3) > 0$ is always fulfilled in the studied spectral range. Figure 1A shows the dispersion of propagating HPhPs, calculated analytically from Eq. 1 (solid line) and by full-wave numerical simulations (dots), along both in-plane crystal directions ([100] and [001], corresponding to the x and y axes) of a 60-nm-thick α-MoO$_3$ slab placed on top of a SiO$_2$ substrate. In this reststrahlen band of α-MoO$_3$, below the longitudinal optical (LO) phonon frequency (28), $\omega_{LO} = 963$ cm^{-1} (Fig. 1A), the α-MoO$_3$/SiO$_2$ heterostructure supports the lowest-order polaritonic mode ($l = 0$) along the [100] crystal direction of α-MoO$_3$, i.e., along the crystal direction with negative permittivity, while there are no polaritonic modes along the dielectric [001] direction, which therefore constitutes a forbidden propagation direction in this spectral range. Hence, the $l = 0$

polaritonic mode exhibits in-plane hyperbolic dispersion, consistently with what has been reported in prior works (16, 17). This hyperbolic dispersion is more clearly visualized by plotting the IFC at a representative incident frequency, $\omega_0 = 934$ cm^{-1} (Fig. 1B). In this case, the IFC is a closed bow tie–shaped curve composed of a finite hyperbola whose major axis lays along $k_{[100]}$ and a crossing through the origin. While the hyperbola describes propagating modes for which $Re(\mathbf{k}) > Im(\mathbf{k})$ (blue lines in Fig. 1B), the crossing represents overdamped modes which fulfill $Im(\mathbf{k}) > Re(\mathbf{k})$ (gray lines in Fig. 1B), the latter regime often overlooked in the literature. Blue and gray dots shown in Fig. 1B are obtained from full-wave numerical simulations, showing an excellent agreement with both parts of the analytical IFC. Hence, the IFC gives rise to propagation of HPhPs within hyperbolic sectors centered along the [100] crystal direction (Fig. 1C). These modes present a slab- or volume-confined propagation, as shown by extracting cross sections of both the near-field distribution $Re(E_z)$ (inset in Fig. 1C) and the norm of the Poynting vector $|\mathbf{S}|$ across the blue-shaded section in Fig. 1C (see section S3).

In contrast, when the α-MoO$_3$ slab is placed on top of 4H-SiC (with air as superstrate, $\varepsilon_1 = 1$), the polaritonic dispersion changes markedly (Fig. 1D). The lowest-order hyperbolic mode $l = 0$ shows now dispersion along either the [100] or the [001] α-MoO$_3$ crystal directions (blue line and dots on the left and right panels of Fig. 1D, respectively), depending on the excitation frequency. In particular, the $l = 0$ mode is observed along the [100] direction between the SO phonon frequency of 4H-SiC, $\omega_{SO} = 943$ cm^{-1}, and the LO phonon frequency of α-MoO$_3$, $\omega_{LO} = 963$ cm^{-1}, i.e., when $Re(\varepsilon_3) > -1$. On the other hand, the $l = 0$ mode emerges along the [001] direction below ω_{SO}, i.e., when $Re(\varepsilon_3) < -1$, where it shows negative phase velocity, $v_p = \omega/k < 0$. Along the [001] direction, the α-MoO$_3$ slab has positive permittivity and, thus, is optically equivalent to a dielectric, whereas the 4H-SiC substrate has negative permittivity and, thus, behaves (optically) as a metal. Hence, surface polaritons exist at the interface α-MoO$_3$/4H-SiC, and their dispersion tends asymptotically to the frequency of the SO phonons at the interfaces α-MoO$_3$/4H-SiC and air/4H-SiC at large and small k, respectively (see section S4) (31). On the other hand, along the [100] direction, no polaritonic mode is supported in this spectral range (see section S1), although both 4H-SiC and α-MoO$_3$ individually support polaritons in this frequency range. Therefore, as a consequence of the α-MoO$_3$ biaxial slab being embedded in an environment, which fulfills the condition $Re(\varepsilon_1) + Re(\varepsilon_3) < 0$, the corresponding IFC of the $l = 0$ mode at $\omega_0 = 934$ cm^{-1} in the α-MoO$_3$/4H-SiC heterostructure is a closed bow tie–shaped curve composed of a finite hyperbola-like curve for propagating modes with its major axis laying now along $k_{[001]}$. We highlight that this anomalous effect is theoretically derived when considering the heterostructure as a whole, not only for the substrate or the slab as separate entities. The emergence of available wave vectors in the mode dispersion along the $k_{[001]}$ axis leads to propagation of HPhPs within hyperbolic sectors centered along the previously nonpolaritonic [001] α-MoO$_3$ crystal direction (Fig. 1F). This reorientation of the IFC clearly illustrates a 90° rotation of the propagation direction of HPhPs in the α-MoO$_3$/4H-SiC heterostructure. HPhPs along the [001] α-MoO$_3$ crystal direction show surface-confined propagation, as observed by extracting cross sections of the near-field distribution $Re(E_z)$ (inset of Fig. 1F) and the norm of the Poynting vector $|\mathbf{S}|$ across the blue-shaded section in Fig. 1F (see section S3).

To experimentally demonstrate this unique rotation of the directional propagation of HPhPs, we assembled both α-MoO$_3$/4H-SiC and
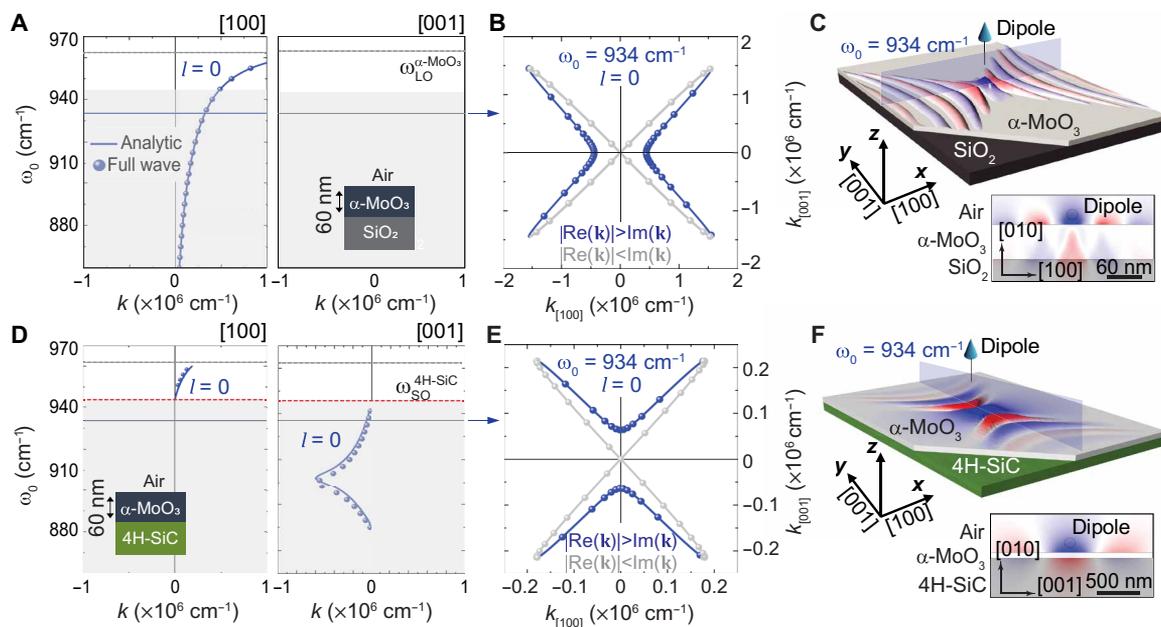
Fig. 1. Rotation of the directional propagation of in-plane HPhPs in an α-MoO₃ biaxial slab. (**A**) Dispersion of HPhPs in a 60-nm-thick α-MoO₃ slab on top of SiO₂ along both in-plane directions. The dashed gray line shows the LO phonon of α-MoO₃, while the continuous blue line marks $\omega_0 = 934$ cm^{-1}. (**B**) IFC of HPhPs propagating in the α-MoO₃/SiO₂ heterostructure at an incident frequency $\omega_0 = 934$ cm^{-1}: The major axis of the hyperbola-like curve lays along $k_{[100]}$. (**C**) Schematics of HPhPs propagating in the α-MoO₃/SiO₂ heterostructure, launched by a dipole source at $\omega_0 = 934$ cm^{-1}. Propagation occurs within hyperbolas centered along the [100] crystal direction of α-MoO₃. The inset shows a cross section of the simulated electric field distribution Re(E_z), revealing that HPhPs in α-MoO₃/SiO₂ are volume-confined. (**D**) Dispersion of HPhPs in a 60-nm-thick α-MoO₃ slab on top of 4H-SiC along both in-plane directions. The dashed gray line shows the LO phonon of α-MoO₃, while the shadowed area indicates the range below the SO phonon of 4H-SiC (dashed red line), also shown in (A) for the sake of comparison. The continuous blue line marks $\omega_0 = 934$ cm^{-1}. (**E**) IFCs of HPhPs propagating in the α-MoO₃/4H-SiC heterostructure at an incident frequency $\omega_0 = 934$ cm^{-1}, showing available wave vectors along $k_{[001]}$. (**F**) Schematics of PhPs propagating in the α-MoO₃/4H-SiC heterostructure, launched by a dipole source at $\omega_0 = 934$ cm^{-1}. Propagation occurs within hyperbolas centered along the [001] crystal direction of α-MoO₃, in stark contrast with that in (C). The inset shows a cross section of the simulated electric field distribution Re(E_z), revealing that HPhPs in α-MoO₃/4H-SiC are surface-confined (see section S3).

α-MoO₃/SiO₂ heterostructures (see Materials and Methods) and compared the propagation of polaritons supported by each of them. Specifically, we performed real-space infrared nanoimaging [using scattering-type near-field optical microscopy (s-SNOM)] of polaritons that are efficiently launched by a metallic antenna (*25*, *32*) fabricated on top of the heterostructures (see schematics in Fig. 2A and Materials and Methods). We acquired near-field amplitude images at an incident laser frequency $\omega_0 = 934$ cm^{-1}, since our theoretical calculations predict that, at this frequency, HPhPs will propagate along orthogonal in-plane directions in these material heterostructures. For the α-MoO₃/SiO₂ system, our images show HPhPs propagating with concave wavefronts within hyperbolic sectors centered along the [100] direction, consistently with prior reports (*16*, *17*) (Fig. 2B, top). However, in the α-MoO₃/4H-SiC heterostructure (Fig. 2C), we observe HPhPs propagating with concave wavefronts within hyperbolic sectors centered along the [001] direction, which has thus far been an intrinsically forbidden polaritonic direction in single slabs of α-MoO₃ (*16*, *17*) in the spectral band of 821.4 to 963.0 cm^{-1}. To further validate these experimental findings, we perform full-wave numerical simulations, where, instead of a metallic antenna, a vertically oriented electric dipole placed on top of the heterostructures acts as the polaritonic source (see Materials and Methods). The obtained near-field simulations show HPhPs propagating along the [100] in-plane direction in the α-MoO₃/SiO₂ heterostructure (Fig. 2B, bottom) and along its [001] orthogonal direction in the α-MoO₃/4H-SiC heterostructure (Fig. 2C, bottom). Together, our results unambiguously

uncover a 90° rotation of the major axis of the polaritonic IFC, corroborating that the directional propagation of in-plane HPhPs in a biaxial slab can be effectively engineered along previously forbidden directions, as predicted by our analytical study. Note that we choose α-MoO₃ flakes of different thicknesses in both heterostructures (360 and 61 nm for α-MoO₃/SiO₂ and α-MoO3/4H-SiC, respectively) so that the wavelengths of HPhPs supported by them are similar, thus facilitating the comparison of the IFCs.

We can gain further insights into the rotation of the IFC by extracting the HPhPs dispersion in each of the heterostructures from near-field measurements at different incident frequencies ω_0, and comparing them to a false color plot of the imaginary part of the Fresnel reflection coefficient, Im($r_p(\omega, k)$), obtained from transfer-matrix calculations (*33*) (Fig. 2, D and E). As expected, the calculated polaritonic dispersion in α-MoO₃/SiO₂ (visible as bright maxima in the color plot) appears only along the [100] crystal direction (Fig. 2D) (*16*, *17*, *28*). In turn, the α-MoO₃/4H-SiC heterostructure shows polaritonic branches along both the [100] crystal direction (Fig. 2E), above ω_{SO}, and [001] crystal direction, below ω_{SO}, i.e., when the permittivity of 4H-SiC takes values below −1, in agreement with our analytical theory (Fig. 1). Besides, as illustrated in Fig. 1D, polaritons exhibit negative phase velocity $v_p = \omega/k$, and a very flat dispersion curve (*31*, *34*) yielding ultraslow group velocities of about 10^{-4} c (see section S5).

To explore in detail the transition occurring between these mutually rotated propagation regimes, we image antenna-launched polaritons
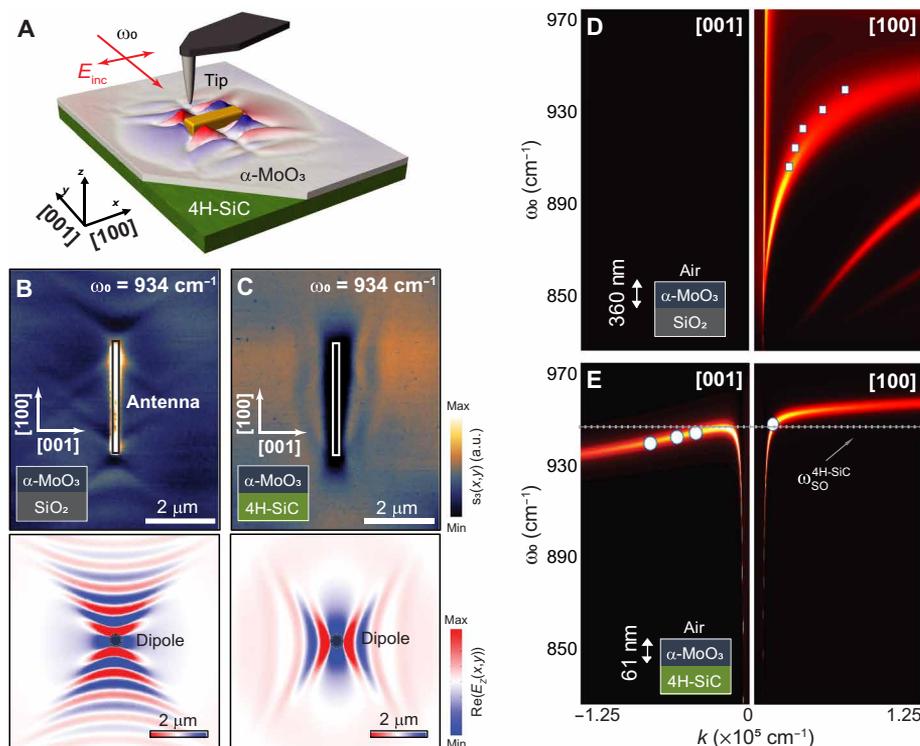
Fig. 2. Visualization of the rotation of the directional propagation of in-plane HPhPs in an α-MoO₃/4H-SiC heterostructure. (**A**) Illustration of antenna-launched HPhPs in an α-MoO₃/4H-SiC heterostructure. The spatial distribution of the near field (shown in red and blue) is adapted from the simulation of the near-field distribution, $Re(E_z(x, y))$. (**B**) Top: Experimental near-field amplitude images $s_3(x, y)$ of antenna-launched HPhPs on a 360-nm-thick α-MoO₃ flake on top of SiO₂ at an incident frequency $\omega_0 = 934$ cm⁻¹. Propagation occurs within hyperbolic sectors centered along the [100] α-MoO₃ crystal direction. Bottom: Simulated near-field distribution, $Re(E_z(x, y))$, excited by a point dipole on a 360-nm-thick α-MoO₃ flake on top of SiO₂ at $\omega_0 = 934$ cm⁻¹. a.u., arbitrary units. (**C**) Top: Experimental near-field amplitude images $s_3(x, y)$ of antenna-launched HPhPs on a 61-nm-thick α-MoO₃ flake on top of 4H-SiC at $\omega_0 = 934$ cm⁻¹. Propagation occurs within hyperbolic sectors centered along the [001] α-MoO₃ crystal direction. Bottom: Simulated near-field distribution, $Re(E_z(x, y))$, excited by a point dipole on a 61-nm-thick α-MoO₃ flake on top of 4H-SiC at $\omega_0 = 934$ cm⁻¹. (**D**) Transfer-matrix calculations (false color plot) of HPhPs propagating on a 360-nm-thick α-MoO₃ flake on top of SiO₂ along the [001] (left) and [100] (right) crystal directions. White dots indicate experimental data from monochromatic s-SNOM imaging. (**E**) Transfer-matrix calculations (false color plot) of HPhPs propagating on a 61-nm-thick α-MoO₃ flake on top of 4H-SiC along the [001] (left) and [100] (right) crystal directions. White dots indicate experimental data from monochromatic s-SNOM imaging. The dashed white line marks the SO phonon of 4H-SiC at $\omega_{SO} = 943$ cm⁻¹.

in the α-MoO₃/4H-SiC heterostructure at several intermediate frequencies between $\omega_0 = 948$ cm⁻¹ and $\omega_0 = 937$ cm⁻¹, i.e., in the frequency range in which the rotation takes place. At the highest frequency, $\omega_0 = 948$ cm⁻¹, we observe HPhPs propagating within a hyperbolic sector whose major axis lays along the [100] α-MoO₃ direction (Fig. 3A). However, when lowering the frequency to $\omega_0 = 943$ cm⁻¹, propagation of HPhPs takes place also within a hyperbolic sector whose major axis lays along the [001] direction (Fig. 3B). This behavior becomes even more evident at a slightly lower frequency, $\omega_0 = 941$ cm⁻¹ (Fig. 3C), where exotic propagation of polaritons within hyperbolic sectors whose major axes lay along both orthogonal directions is clearly seen. Last, by further lowering the frequency to $\omega_0 = 937$ cm⁻¹, propagation of polaritons is only observed within a hyperbolic sector whose major axis lays along the [001] crystal direction (Fig. 3D), thus completing a 90° rotation from the initial directional propagation of HPhPs at $\omega_0 = 948$ cm⁻¹.

We perform additional theoretical analyses to understand this exotic behavior of propagating polaritons. Namely, we numerically calculate the near-field distributions $Re(E_z(x, y))$ generated at the aforementioned frequencies by a localized source placed above a 61-nm-thick α-MoO₃ flake on top of 4H-SiC, and subsequently, we

Fourier-transform (FT) them (left of Fig. 3, E to H). The resulting FTs clearly show the rotation of the major axes of the hyperbolic IFCs from the [100] to the [001] α-MoO₃ crystal directions when comparing the furthermost cases at $\omega_0 = 948$ and 937 cm⁻¹. However, apart from the rotation effect, the FTs also show nontrivial features appearing at intermediate frequencies, $\omega_0 = 943$ and 941 cm⁻¹, and relatively low momenta (Fig. 3, F and G). Although these features suggest a complicated multimode excitation in this frequency range, by performing a careful analysis of the generated field patterns based on the dyadic Green's function and simplified dispersion relations (see section S6), we find that only two modes excited in the heterostructure present a major contribution to the fields launched by a localized source: the lowest-order mode ($l = 0$, according to Eq. 1) and the mode arising under the limit of a vanishing slab thickness $d \to 0$ (see Materials and Methods). Hence, we can describe properly the main nontrivial features of the FTs in this frequency range in terms of the real part of the analytical IFCs of these two modes (see section S7). Namely, the branches of the hyperbolic IFC of the mode $l = 0$ linearize and intersect in one point at one specific frequency (blue curve in the right of Fig. 3F), and wave vectors with small modulus become available along all in-plane directions for the $d \to 0$ mode (red curve in the right of Fig. 3F),
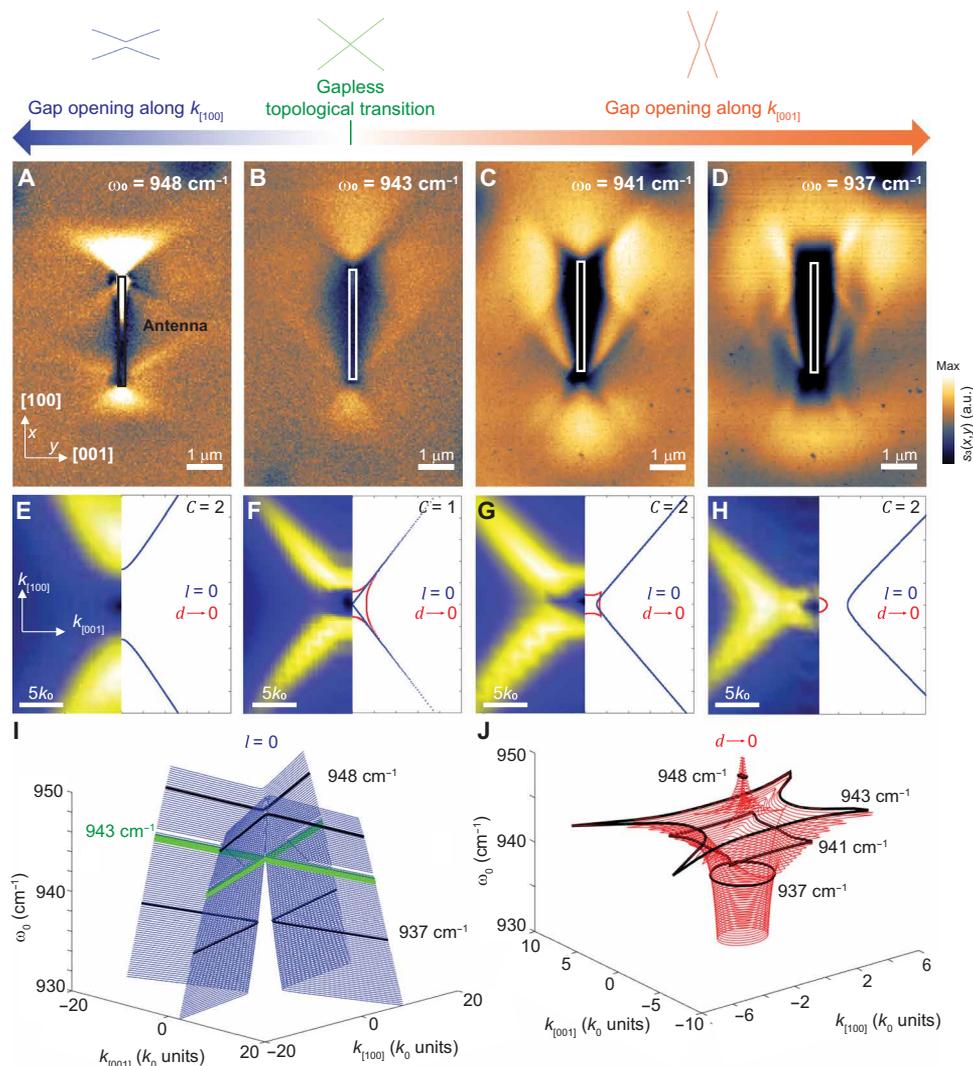
Fig. 3. Topological transition of the polaritonic IFC between orthogonal hyperbolic regimes in an α-MoO₃/4H-SiC heterostructure. (**A** to **D**) Experimental near-field amplitude images $s_3(x, y)$ of antenna-launched hyperbolic PhPs on a 61-nm-thick α-MoO₃ flake on top of 4H-SiC at different illuminating frequencies. (**E** to **H**) Left: Simulated IFCs, calculated by Fourier-transforming simulated near-field distributions, $Re(E_z(x, y))$ created by a point dipole on a 61-nm-thick α-MoO₃ flake on top of 4H-SiC. Right: Analytical IFCs for the fundamental mode $l = 0$ (blue) and the mode $d \rightarrow 0$ (red). (**I** and **J**) 3D visualization of the topological transition of the fundamental mode $l = 0$ and of the mode $d \rightarrow 0$, in blue and red, respectively. Black lines show the IFCs at the frequencies at which the near-field images were acquired. The green line depicts the IFC at the topological transition.

It is worth having a look at the path connectedness, i.e., the number of components in which a path can be drawn between any two points of the curve within it, of the analytical real-part IFCs for the $l = 0$ mode, as it is one of the main properties that are used to distinguish different topological spaces. Unlike size or shape, path connectedness remains unchanged under homeomorphisms, and thus, based on it, we can distinguish when two curves are not topologically equivalent, i.e., not homeomorphic. At $\omega_0 = 948, 941$, and 937 cm^{-1} the number of path-connected components C of the IFC of the $l = 0$ mode is 2. However, at $\omega_0 = 943$ cm^{-1}, the gap in the IFC notably closes, and the number of path-connected components of the IFC evolves from $C = 2$ to $C = 1$. This IFC gap opening/closing of the IFC corresponds to cutting/attaching the polaritonic dispersion in momentum space and alters the topology of the system (*35*), as it represents a discontinuous deformation that can be mapped as an

abrupt change of a topological parameter of the polaritonic mode $l = 0$ (see section S8). This unveils one of the hallmark features of the three-dimensional (3D) polaritonic topological transition that emerges for the IFC of the lowest-order polaritonic mode in the frequency range between both mutually rotated regimes in the α-MoO₃/4H-SiC heterostructure. This transition can thus be more clearly visualized in a 3D plot of the in-plane dispersion of the IFC as a function of frequency ω, i.e., in the 3D space (k_x, k_y, ω) (Fig. 3I). The resulting surface is a hyperbolic cylinder composed of two disconnected sheets with their in-plane major axes along the $k_{[001]}$ direction at low frequencies and along the $k_{[100]}$ direction at high frequencies, respectively. These sheets become connected at the transition frequency $\omega_0 = 943$ cm^{-1}, forming a cross-like curve (depicted in green) and clearly illustrating the topological transition of the IFC. The crossing point constitutes a degeneracy between topologically inequivalent

IFCs, akin to a Weyl point in electronic band structures (*35*). In Fig. 3J, we show a 3D plot of the mode $d \to 0$ as a function of frequency ω, a surface composed of closed IFCs with low momentum. The cross sections of this surface markedly change as a function of frequency (from a circle-like to a four-vertex star-like IFC) although preserving the same topology up to $\omega_0 = 943$ cm^{-1}, where the surface virtually collapses into a point. Thus, the mode $l = 0$ undergoes a topological transition in this frequency range, while the mode $d \to 0$ does not. However, we attribute the peculiarities observed in near-field images in Fig. 3 (A to D) to the strong frequency dependence of the propagation direction of polaritons, manifesting itself as a robust change of the IFCs of both $l = 0$ and $d \to 0$ modes, particularly in the vicinity of the topological transition frequency.

To sum up, we report on the engineering of the directional propagation of low-loss HPhPs in a natural medium along intrinsically forbidden directions, driven by an optical topological transition that emerges when the crystal lays on a substrate with a specific negative permittivity. Contrary to other expected polaritonic topological transitions, as those at the spectral limits between reststrahlen bands, and thereby close to transverse optical phonons where losses in the medium are high, the topological transition here reported when α-MoO$_3$ is placed on 4H-SiC takes place at $\omega_{SO} = 943$ cm^{-1}, where losses are low and thus optimal visualization of its unique features can be carried out in real space. In turn, our results reveal two different regimes in which HPhPs propagate along mutually orthogonal directions, including the naturally forbidden [001] crystal direction for polaritonic propagation in bare α-MoO$_3$ in the studied spectral range, and exotic intermediate states that unveil the topological origin of the transition, where HPhPs propagate within hyperbolas centered along both the [001] and [100] α-MoO$_3$ directions. Our work opens up stimulating horizons for the investigation of topology-related features in polaritons in vdW materials, such as the existence of edge states (*36*), topologically protected states, or the study of nodal points in momentum space protected by symmetries. In addition, extensive and effective control of the propagation of hyperbolic polaritons at the nanoscale is potentially possible via hybridization with plasmon polaritons (*37*) in various polaritonic heterostructures, thanks to the growing palette of polaritonic vdW materials that sum up to other conventional polaritonic media, such as SiC, aluminum nitride (AlN), or quartz. Furthermore, the introduction of new degrees of freedom—such as the twist angle (*24–27*)—and controlled external stimuli—such as elastic strain, electric doping, or photoinjection of carriers—can enable further external tuning of the propagation direction and the control of optical topological transitions naturally emerging in polaritonic heterostructures. In this context, our findings promise new opportunities for developing mid-infrared and terahertz (*38*) optical devices and for manipulating the flow of light at the nanoscale with unprecedented degree of control. Moreover, this study provides fundamentally relevant insights into the emergence of optical topological transitions in low-loss vdW crystals, as well as a pathway through which to translate recent developments in topological engineering in low-dimensional electronic materials to photonics and polaritonics.

MATERIALS AND METHODS

Fabrication of heterostructures
Bulk α-MoO$_3$ crystals were thinned down from commercial bulk materials (Alfa Aesar) by mechanical exfoliation using Nitto blue tape, yielding thin slabs with thicknesses between 60 nm and a few micrometres. A second exfoliation of the α-MoO$_3$ flakes from the tape to a transparent polydimethylsiloxane (PDMS) stamp was performed. The transferred flakes were inspected with an optical microscope to select homogeneous and large pieces with the desired thickness. The α-MoO$_3$ flakes were peeled off from the PDMS to SiO$_2$/Si and 4H-SiC substrates. For maximum yield of thin crystals, they were heated to 200°C during the transfer.

Fabrication of gold antennas
High-resolution electron beam lithography (100 kV and 100 pA) was carried out with submicrometer alignments on our samples coated with a poly(methyl methacrylate) resist layer. With conventional high-resolution developer [1:3 methyl isobutyl ketone:isopropyl alcohol (IPA)], evaporation of 5-nm Cr and 30-nm Au and a lift-off were performed to define the antennas. To remove any organic residual, we performed a hot acetone bath at 60°C for 10 to 15 min and a gentle rinse of IPA for 1 min, followed by a nitrogen gas drying and thermal evaporation. The dimensions of gold antenna were 3 μm (length) by 50 nm (width) by 40 nm (height). We note that α-MoO$_3$ layers are sensitive to any ultrasonic processing.

Scattering-type scanning near-field optical microscopy
Infrared nanoimaging was performed using a commercially available s-SNOM (from Neaspec) where a metalized (Pt-coated) cantilevered atomic force microscope tip is used as a scattering near-field probe. The tip oscillates vertically at the mechanical resonant frequency of the cantilever (around 270 kHz), with an amplitude of about 50 nm. The sample is illuminated with *s*-polarized infrared light at frequency ω_0 (from tunable CO$_2$ and quantum cascade lasers). The electric fields are concentrated at the two apexes of the resonant dipolar gold antennas, so that each of them acts as a point dipole. The tip-scattered field is recorded with a pseudo-heterodyne Michelson interferometer. Demodulation of the interferometric detector signal at the *n*th harmonics of the tip oscillation frequency allows us to subtract the background signal, yielding the complex-valued near-field signals $\sigma_n = s_n e^{i\phi_n}$, s_n, and ϕ_n being the near-field amplitude and phase, respectively. In this work, we demodulated the near-field signal at the third harmonic of the tapping frequency. By recording the near-field signals as a function of the lateral tip position, we obtain near-field images.

Full-wave numerical simulations
Full-wave numerical simulations were performed to calculate the real part of the vertical component of the near-field Re($E_z(x, y)$), using the finite boundary elements method COMSOL Multiphysics. The structures were modeled as α-MoO$_3$ biaxial slabs on top of SiO$_2$ or 4H-SiC substrates, and PhPs were launched by vertically oriented electric point dipole sources placed on top of them, accurately reproducing the polaritonic patterns launched by the apexes of the dipolar nanoantennas in our experimental images. The vertical or horizontal orientation of the polariton sources only plays a role in the directionality of the launched waves (see section S9). Therefore, to avoid asymmetric patterns, we have used vertical dipoles in our simulations. Furthermore, the permittivity values for α-MoO$_3$ and 4H-SiC used throughout the work were taken from (*28*) and (*30*), respectively, while those for SiO$_2$ were taken from (*39*) and adapted to account for our near-field experimental data. We have considered 4H-SiC to be isotropic throughout the work (see section S10).

Analytical dispersion of polaritons in the thin-film limit

Polaritons in ultrathin slabs and monolayers have recently attracted much attention (*16, 25, 29, 40–43*). Therefore, the limit of a vanishing slab thickness $d \rightarrow 0$ is of a great practical interest. As already reported in the literature (*16, 28*), by assuming that all the components of the dielectric tensor $\hat{\varepsilon}$ are large, i.e., $|\varepsilon_i| \gg 1$ ($i = x, y, z$) and approximating the slab of a finite thickness by a 2D conductive sheet, with effective conductivity $\hat{\sigma}$ given by $\hat{\sigma} = \omega d \hat{\varepsilon}/4\pi i$, the dispersion relation of polaritons propagating in ultrathin films can be obtained

$$\left[\alpha_x q_y^2 + \alpha_y q_x^2 + i \frac{q_x^2 + q_y^2}{2} (q_{1z} + q_{3z}) \right]$$

$$\left[\alpha_x q_x^2 + \alpha_y q_y^2 - i \frac{q_x^2 + q_y^2}{2} \left(\frac{\varepsilon_1}{q_{1z}} + \frac{\varepsilon_3}{q_{3z}} \right) \right] = q_x^2 q_y^2 (\alpha_x - \alpha_y)^2$$

where $\alpha_{x, y} = k_0 d \varepsilon_{x, y}/2i$ is the normalized 2D effective conductivity components, $q_{x, y} = k_{x, y}/k_0$ is the in-plane components of the normalized wave vector, and $q_{1,3z} = \sqrt{q^2 - \varepsilon_{1,3}}$, with $q = \sqrt{q_x^2 + q_y^2}$. This dispersion relation, written for biaxial slabs of small but nonzero thickness (the effective conductivities $\alpha_{x, y}$ are thickness dependent), has already been used for the analysis of hyperbolic PhPs in thin slabs of α-MoO$_3$ (*16*). This equation does not require the assumption of high q, but it gives only zero-order modes with different polarizations, in contrast to Eq. 1, which describes only one polarization (Transverse magnetic).

SUPPLEMENTARY MATERIALS

Supplementary material for this article is available at http://advances.sciencemag.org/cgi/content/full/7/14/eabf2690/DC1

REFERENCES AND NOTES

1. T. Low, A. Chaves, J. D. Caldwell, A. Kumar, N. X. Fang, P. Avouris, T. F. Heinz, F. Guinea, L. Martin-Moreno, F. Koppens, Polaritons in layered two-dimensional materials. *Nat. Mater.* **16**, 182–194 (2017).
2. D. N. Basov, M. M. Fogler, F. J. García de Abajo, Polaritons in van der Waals materials. *Science* **354**, aag1992 (2016).
3. J. D. Caldwell, L. Lindsay, V. Giannini, I. Vurgaftman, T. L. Reinecke, S. A. Maier, O. J. Glembocki, Low-loss, infrared and terahertz nanophotonics using surface phonon polaritons. *Nanophotonics* **4**, 44–68 (2015).
4. A. Poddubny, I. Iorsh, P. Belov, Y. Kivshar, Hyperbolic metamaterials. *Nat. Photonics* **7**, 958–967 (2013).
5. P. Li, I. Dolado, F. J. Alfaro-Mozaz, F. Casanova, L. E. Hueso, S. Liu, J. H. Edgar, A. Y. Nikitin, S. Vélez, R. Hillenbrand, Infrared hyperbolic metasurface based on nanostructured van der Waals materials. *Science* **359**, 892–896 (2018).
6. G. Hu, J. Shen, C.-W. Qiu, A. Alù, S. Dai, Phonon polaritons and hyperbolic response in van der Waals materials. *Adv. Opt. Mater.* **8**, 1901393 (2020).
7. C. Wang, S. Huang, Q. Xing, Y. Xie, C. Song, F. Wang, H. Yan, Van der Waals thin films of WTe$_2$ for natural hyperbolic plasmonic surfaces. *Nat. Commun.* **11**, 1158 (2020).
8. T. Repän, O. Takayama, A. V. Lavrinenko, Wave front tuning of coupled hyperbolic surface waves on anisotropic interfaces. *Photonics* **7**, 34 (2020).
9. S. Dai, Z. Fei, Q. Ma, A. S. Rodin, M. Wagner, A. S. McLeod, M. K. Liu, W. Gannett, W. Regan, K. Watanabe, T. Taniguchi, M. Thiemens, G. Dominguez, A. H. C. Neto, A. Zettl, F. Keilmann, P. Jarillo-Herrero, M. M. Fogler, D. N. Basov, Tunable phonon polaritons in atomically thin van der Waals crystals of boron nitride. *Science* **343**, 1125–1129 (2014).
10. A. J. Giles, S. Dai, I. Vurgaftman, T. Hoffman, S. Liu, L. Lindsay, C. T. Ellis, N. Assefa, I. Chatzakis, T. L. Reinecke, J. G. Tischler, M. M. Fogler, J. H. Edgar, D. N. Basov, J. D. Caldwell, Ultralow-loss polaritons in isotopically pure boron nitride. *Nat. Mater.* **17**, 134–139 (2018).
11. J. D. Caldwell, A. V. Kretinin, Y. Chen, V. Giannini, M. M. Fogler, Y. Francescato, C. T. Ellis, J. G. Tischler, C. R. Woods, A. J. Giles, M. Hong, K. Watanabe, T. Taniguchi, S. A. Maier, K. S. Novoselov, Sub-diffractional volume-confined polaritons in the natural hyperbolic material hexagonal boron nitride. *Nat. Commun.* **5**, 5221 (2014).
12. J. D. Caldwell, I. Aharonovich, G. Cassabois, J. H. Edgar, B. Gil, D. N. Basov, Photonics with hexagonal boron nitride. *Nat. Rev. Mater.* **4**, 552–567 (2019).
13. S. Dai, Q. Ma, T. Andersen, A. S. Mcleod, Z. Fei, M. K. Liu, M. Wagner, K. Watanabe, T. Taniguchi, M. Thiemens, F. Keilmann, P. Jarillo-Herrero, M. M. Fogler, D. N. Basov, Subdiffractional focusing and guiding of polaritonic rays in a natural hyperbolic material. *Nat. Commun.* **6**, 6963 (2015).
14. P. Li, M. Lewin, A. V. Kretinin, J. D. Caldwell, K. S. Novoselov, T. Taniguchi, K. Watanabe, F. Gaussmann, T. Taubner, Hyperbolic phonon-polaritons in boron nitride for near-field optical imaging and focusing. *Nat. Commun.* **6**, 7507 (2015).
15. M. Autore, P. Li, I. Dolado, F. J. Alfaro-Mozaz, R. Esteban, A. Atxabal, F. Casanova, L. E. Hueso, P. Alonso-González, J. Aizpurua, A. Y. Nikitin, S. Vélez, R. Hillenbrand, Boron nitride nanoresonators for phonon-enhanced molecular vibrational spectroscopy at the strong coupling limit. *Light Sci. Appl.* **7**, 17172 (2018).
16. W. Ma, P. Alonso-González, S. Li, A. Y. Nikitin, J. Yuan, J. Martín-Sánchez, J. Taboada-Gutiérrez, I. Amenabar, P. Li, S. Vélez, C. Tollan, Z. Dai, Y. Zhang, S. Sriram, K. Kalantar-Zadeh, S.-T. Lee, R. Hillenbrand, Q. Bao, In-plane anisotropic and ultra-low-loss polaritons in a natural van der Waals crystal. *Nature* **562**, 557–562 (2018).
17. Z. Zheng, N. Xu, S. L. Oscurato, M. Tamagnone, F. Sun, Y. Jiang, Y. Ke, J. Chen, W. Huang, W. L. Wilson, A. Ambrosio, S. Deng, H. Chen, A mid-infrared biaxial hyperbolic van der Waals crystal. *Sci. Adv.* **5**, eaav8690 (2019).
18. J. Taboada-Gutiérrez, G. Álvarez-Pérez, J. Duan, W. Ma, K. Crowley, I. Prieto, A. Bylinkin, M. Autore, H. Volkova, K. Kimura, T. Kimura, M.-H. Berger, S. Li, Q. Bao, X. P. A. Gao, I. Errea, A. Y. Nikitin, R. Hillenbrand, J. Martín-Sánchez, P. Alonso-González, Broad spectral tuning of ultra-low-loss polaritons in a van der Waals crystal by intercalation. *Nat. Mater.* **19**, 964–968 (2020).
19. E. Bermúdez-Ureña, C. Gonzalez-Ballestero, M. Geiselmann, R. Marty, I. P. Radko, T. Holmgaard, Y. Alaverdyan, E. Moreno, F. J. García-Vidal, S. I. Bozhevolnyi, R. Quidant, Coupling of individual quantum emitters to channel plasmons. *Nat. Commun.* **6**, 7883 (2015).
20. C. L. Cortes, Z. Jacob, Super-Coulombic atom–atom interactions in hyperbolic media. *Nat. Commun.* **8**, 14144 (2017).
21. L. Tranchant, S. Hamamura, J. Ordonez-Miranda, T. Yabuki, A. Vega-Flick, F. Cervantes-Alvarez, J. J. Alvarado-Gil, S. Volz, K. Miyazaki, Two-dimensional phonon polariton heat transport. *Nano Lett.* **19**, 6924–6930 (2019).
22. K. Chaudhary, M. Tamagnone, M. Rezaee, D. K. Bediako, A. Ambrosio, P. Kim, F. Capasso, Engineering phonon polaritons in van der Waals heterostructures to enhance in-plane optical anisotropy. *Sci. Adv.* **5**, eaau7171 (2019).
23. P. Li, G. Hu, I. Dolado, M. Tymchenko, C.-W. Qiu, F. J. Alfaro-Mozaz, F. Casanova, L. E. Hueso, S. Liu, J. H. Edgar, S. Vélez, A. Alu, R. Hillenbrand, Collective near-field coupling and nonlocal phenomena in infrared-phononic metasurfaces for nano-light canalization. *Nat. Commun.* **11**, 3663 (2020).
24. G. Hu, Q. Ou, G. Si, Y. Wu, J. Wu, Z. Dai, A. Krasnok, Y. Mazor, Q. Zhang, Q. Bao, C.-W. Qiu, A. Alù, Topological polaritons and photonic magic angles in twisted α-MoO$_3$ bilayers. *Nature* **582**, 209–213 (2020).
25. J. Duan, N. Capote-Robayna, J. Taboada-Gutiérrez, G. Álvarez-Pérez, I. Prieto, J. Martín-Sánchez, A. Y. Nikitin, P. Alonso-González, Twisted nano-optics: Manipulating light at the nanoscale with twisted phonon polaritonic slabs. *Nano Lett.* **20**, 5323–5329 (2020).
26. M. Chen, X. Lin, T. H. Dinh, Z. Zheng, J. Shen, Q. Ma, H. Chen, P. Jarillo-Herrero, S. Dai, Configurable phonon polaritons in twisted α-MoO$_3$. *Nat. Mater.* **19**, 1307–1311 (2020).
27. Z. Zheng, F. Sun, W. Huang, J. Jiang, R. Zhan, Y. Ke, H. Chen, S. Deng, Phonon polaritons in twisted double-layers of hyperbolic van der Waals crystals. *Nano Lett.* **20**, 5301–5308 (2020).
28. G. Álvarez-Pérez, T. G. Folland, I. Errea, J. Taboada-Gutiérrez, J. Duan, J. Martín-Sánchez, A. I. F. Tresguerres-Mata, J. R. Matson, A. Bylinkin, M. He, W. Ma, Q. Bao, J. I. Martín, J. D. Caldwell, A. Y. Nikitin, P. Alonso-González, Infrared permittivity of the biaxial van der waals semiconductor α-MoO$_3$ from near- and far-field correlative studies. *Adv. Mater.* **32**, 1908176 (2020).
29. G. Álvarez-Pérez, K. V. Voronin, V. S. Volkov, P. Alonso-González, A. Y. Nikitin, Analytical approximations for the dispersion of electromagnetic modes in slabs of biaxial crystals. *Phys. Rev. B* **100**, 235408 (2019).
30. T. E. Tiwald, J. A. Woollam, S. Zollner, J. Christiansen, R. B. Gregory, T. Wetteroth, S. R. Wilson, A. R. Powell, Carrier concentration and lattice absorption in bulk and epitaxial silicon carbide determined using infrared ellipsometry. *Phys. Rev. B* **60**, 11464–11474 (1999).
31. A. Karalis, E. Lidorikis, M. Ibanescu, J. D. Joannopoulos, M. Soljačić, Surface-plasmon-assisted guiding of broadband slow and subwavelength light in air. *Phys. Rev. Lett.* **95**, 063901 (2005).
32. P. Pons-Valencia, F. J. Alfaro-Mozaz, M. M. Wiecha, V. Biolek, I. Dolado, S. Vélez, P. Li, P. Alonso-González, F. Casanova, L. E. Hueso, L. Martín-Moreno, R. Hillenbrand, A. Y. Nikitin, Launching of hyperbolic phonon-polaritons in h-BN slabs by resonant metal plasmonic antennas. *Nat. Commun.* **10**, 3242 (2019).
33. N. C. Passler, A. Paarmann, Generalized 4 × 4 matrix formalism for light propagation in anisotropic stratified media: Study of surface phonon polaritons in polar dielectric heterostructures. *J. Opt. Soc. Am. B* **34**, 2128–2139 (2017).
34. P. Li, X. Yang, T. W. W. Maß, J. Hanss, M. Lewin, A.-K. U. Michel, M. Wuttig, T. Taubner, Reversible optical switching of highly confined phonon–polaritons with an ultrathin phase-change material. *Nat. Mater.* **15**, 870–875 (2016).

35. M. Kim, Z. Jacob, J. Rho, Recent advances in 2D, 3D and higher-order topological photonics. *Light Sci. Appl.* **9**, 130 (2020).

36. A. A. Sokolik, O. V. Kotov, Y. E. Lozovik, Plasmonic-like modes at inclined edges of anisotropic 2D materials. arXiv:2011.13480 [cond-mat.mes-hall] (25 November 2020).

37. S. Dai, Q. Ma, M. K. Liu, T. Andersen, Z. Fei, M. D. Goldflam, M. Wagner, K. Watanabe, T. Taniguchi, M. Thiemens, F. Keilmann, G. C. A. M. Janssen, S.-E. Zhu, P. Jarillo-Herrero, M. M. Fogler, D. N. Basov, Graphene on hexagonal boron nitride as a tunable hyperbolic metamaterial. *Nat. Nanotechnol.* **10**, 682–686 (2015).

38. T. V. A. G. de Oliveira, T. Nörenberg, G. Álvarez-Pérez, L. Wehmeier, J. Taboada-Gutiérrez, M. Obst, F. Hempel, E. J. H. Lee, J. M. Klopf, I. Errea, A. Y. Nikitin, S. C. Kehr, P. Alonso-González, L. M. Eng, Nanoscale-confined terahertz polaritons in a van der Waals crystal. *Adv. Mater.* **33**, 2005777 (2021).

39. E. D. Palik, *Handbook of Optical Constants of Solids* (Academic Press, 1998), vol. 3.

40. J. S. Gómez-Díaz, M. Tymchenko, A. Alù, Hyperbolic plasmons and topological transitions over uniaxial metasurfaces. *Phys. Rev. Lett.* **114**, 233901 (2015).

41. A. Y. Nikitin, Graphene plasmonics, in *World Scientific Handbook of Metamaterials and Plasmonics, World Scientific Series in Nanoscience and Nanotechnology* (Cambridge Univ. Press, 2017), vol. 4, chap. 8, pp. 307–338.

42. V. Agranovich, D. Mills, *Surface Polaritons - Electromagnetic Waves at Surfaces and Interfaces* (North Holland, 1982).

43. F. J. Alfaro-Mozaz, S. G. Rodrigo, P. Alonso-González, S. Vélez, I. Dolado, F. Casanova, L. E. Hueso, L. Martín-Moreno, R. Hillenbrand, A. Y. Nikitin, Deeply subwavelength phonon-polaritonic crystal made of a van der Waals material. *Nat. Commun.* **10**, 42 (2019).

44. L. Novotny, B. Hecht, *Principles of Nano-Optics* (Cambridge Univ. Press, 2012).

45. A. Y. Nikitin, F. J. Garcia-Vidal, L. Martin-Moreno, Analytical expressions for the electromagnetic dyadic Green's function in graphene and thin Layers. *IEEE J. Sel. Top. Quantum Electron.* **19**, 4600611 (2013).

46. F. Wijnands, J. B. Pendry, F. J. García-Vidal, P. M. Bell, P. J. Roberts, L. Martín Moreno, Green's functions for Maxwell's equations: Application to spontaneous emission. *Opt. Quant. Electron.* **29**, 199–216 (1997).

Citation: J. Duan, G. Álvarez-Pérez, K. V. Voronin, I. Prieto, J. Taboada-Gutiérrez, V. S. Volkov, J. Martín-Sánchez, A. Y. Nikitin, P. Alonso-González, Enabling propagation of anisotropic polaritons along forbidden directions via a topological transition. *Sci. Adv.* **7**, eabf2690 (2021).

Science Advances

Enabling propagation of anisotropic polaritons along forbidden directions via a topological transition

J. Duan, G. Álvarez-Pérez, K. V. Voronin, I. Prieto, J. Taboada-Gutiérrez, V. S. Volkov, J. Martín-Sánchez, A. Y. Nikitin and P. Alonso-González

ARTICLE TOOLS	http://advances.sciencemag.org/content/7/14/eabf2690
SUPPLEMENTARY MATERIALS	http://advances.sciencemag.org/content/suppl/2021/03/29/7.14.eabf2690.DC1
REFERENCES	This article cites 41 articles, 5 of which you can access for free http://advances.sciencemag.org/content/7/14/eabf2690#BIBL
PERMISSIONS	http://www.sciencemag.org/help/reprints-and-permissions

Use of this article is subject to the Terms of Service